Article

Dual-anion ionic liquid electrolyte enables stable Ni-rich cathodes in lithium-metal batteries

$LiNi_{0.88}Co_{0.09}Mn_{0.03}O_2$
(After cycling)

LP30

ILE

FSI⁻   TFSI⁻

Fanglin Wu, Shan Fang, Matthias Kuenzel, ..., Thomas Diemant, Guk-Tae Kim, Stefano Passerini

guk-tae.kim@kit.edu (G.-T.K.)
stefano.passerini@kit.edu (S.P.)

Highlights

Co-poor Ni-rich layered cathodes (NCM88) for LMBs

Application of a highly stable ILE in LMBs

Long-term performance of high-energy positive-electrode material in ILE

Performance of high-energy Li| NCM88|ILE cells employing thin Li electrode

Exploiting the high-energy density of lithium metal as a negative electrode for lithium batteries is considered a prerequisite to satisfy the continually increasing demand for extended driving range of electric vehicles and fully electrify our mobility and transportation. However, such lithium-metal batteries face critical safety and life-span concerns. This work outlines a clear route toward realizing safe high-energy-density lithium-metal batteries with excellent cycling stability through the use of a non-flammable and low-volatile ionic liquid electrolyte.

Joule

Article

Dual-anion ionic liquid electrolyte enables stable Ni-rich cathodes in lithium-metal batteries

Fanglin Wu,[1,2] Shan Fang,[1,2] Matthias Kuenzel,[1,2] Angelo Mullaliu,[1,2] Jae-Kwang Kim,[3] Xinpei Gao,[1,2] Thomas Diemant,[1,2] Guk-Tae Kim,[1,2,*] and Stefano Passerini[1,2,4,*]

SUMMARY

High-energy-density lithium-metal batteries face the challenge of developing functional electrolytes enabling both the stabilization of the lithium-metal negative electrode and high-voltage positive electrodes (> 4 V versus Li$^+$/Li). Herein, a low-volatility and non-flammable ionic liquid electrolyte (ILE) incorporating two anions, bis(fluorosulfonyl) imide (FSI) and bis(trifluoromethanesulfonyl) imide (TFSI), is successfully applied to overcome this challenge, employing the high-energy, low-Co, and Ni-rich positive-electrode material, LiNi$_{0.88}$Co$_{0.09}$Mn$_{0.03}$O$_2$ (NCM88), in Li-metal batteries. With this specific electrolyte, the cathode exhibits remarkable electrochemical performance, achieving an initial specific capacity of 214 mAh g^{-1} and outstanding capacity retention of 88% over 1,000 cycles. More importantly, this electrolyte enables an average Coulombic efficiency of 99.94%. The excellent compatibility of the dual-anion ILE with both the lithium metal (50 μm) and the high-voltage positive-electrode material enables the realization of Li-metal cells achieving specific energies of more than 560 Wh kg^{-1} based on their combined active material masses.

INTRODUCTION

High-energy batteries, in particular lithium batteries, are the key to achieve carbon-neutral mobility. The already great research efforts in lithium-ion batteries (LIBs) have been further amplified by the fast-growing electric vehicles market.[1] Among the investigated battery chemistries, nickel-rich, layered transition metal oxides appear very promising owing to their high specific capacity[2] and, possibly, very low cobalt content, i.e., meeting the strict necessity of reducing the cobalt proportion in the positive-electrode material due to its limited reserves and strong environmental and ecological concerns.[3] However, the increased nickel content introduces new challenges, such as poor cycling and thermal instability.[4] Regarding the rapid capacity fade, mainly two aspects have been identified as the detrimental factors. The first one is associated to the parasitic reactions occurring at the positive-electrode/electrolyte interface at high state of charge, i.e., when the positive electrode is fully delithiated. The highly reactive Ni^{4+} accelerates the electrolyte decomposition and leads to thickening and parasitic growth of the cathode electrolyte interphase (CEI) constituted by a range of decomposition products.[5] On the other hand, due to the similar ionic radius of Ni^{2+}(0.069 nm) and Li$^+$(0.076 nm), nickel ions can easily migrate from the transition metal layer into neighboring lithium vacancies in the highly delithiated state of the Ni-rich cathodes. This generates a disordered phase,[6] where the narrowed space between the metal oxide slabs is detrimental for lithium-ion diffusion, while at the same time, the displaced transition

Context & scale

High-energy batteries, in particular lithium batteries, are the key to achieve carbon-neutral mobility. Current lithium-ion batteries have already enabled a fast-growing electric vehicles market. However, it is foreseen that a fully electrified mobility and transportation can only be achieved by the development of batteries employing lithium metal as the negative electrode while still granting long-term cycling performance and safety. In this work, the outstanding long-term cycling performance of a Li-metal battery employing the Co-poor and Ni-rich (LiNi$_{0.88}$Co$_{0.09}$Mn$_{0.03}$O$_2$, NCM88) positive-electrode material is demonstrated via the use of a dual-anion ionic liquid electrolyte (0.8Pyr$_{14}$FSI-0.2LiTFSI, ILE). This electrolyte enables initial specific capacity of 214 mAh g^{-1} and outstanding capacity retention of 88% over 1,000 cycles with an average Coulombic efficiency of 99.94%. The Li|ILE|NCM88 cells achieve a specific energy above 560 Wh kg^{-1} based on the combined active material masses.

CellPress
OPEN ACCESS

Joule
Article

metal ions in the lithium layer additionally hinder Li$^+$ diffusion.[2,7] The formation of microcracks is also related to structural rearrangements at high state of charge. The phase transformation from H2 to H3 phase at potentials above 4.0 V is accompanied by large anisotropic volume changes causing microcracks at the phase boundaries between the crystallites in the secondary Ni-rich NCM (LiNi$_{1-x-y}$Co$_x$Mn$_y$)O$_2$ particles.[8] During cycling these microcracks propagate inward from the particle surface and create pathways for the electrolyte to come in contact with freshly exposed highly reactive Ni^{4+}, drastically aggravating electrolyte decomposition and the formation of a NiO-like impurity phase.[4]

Despite these drawbacks of Ni-rich cathodes, substantial efforts have been devoted toward designing materials with the ideal balance of high specific capacity and high safety characteristics required by the market. Thereby, common strategies rely on lattice doping into the transition metal layer to enhance the structural stability of the cathodes.[9] Typically, dopant elements, such as Mg,[10] Ca,[11] Al,[12] and Ti,[13,14] are intended to prevent Ni^{2+} migration into the lithium layer[15] and to strengthen the metal-oxygen bonding in order to restrain oxygen release and improve the thermal stability.[7] Another approach to mitigate the performance decay of such cathode materials is the application of a protective surface coating. This should prevent direct contact between the cathode active materials and the electrolyte, reduce the negative impact of the attack by highly reactive hydrogen fluoride (HF) or some other components, and, thus, alleviate the parasitic reactions stimulated by the presence of Ni^{4+}. Besides, this limits the exposure of the sensitive Ni-rich materials toward moisture and CO$_2$ and, thus, prevents the formation of Li-containing residuals on the particle surface, which would react with the electrolyte and accelerate cell aging.[2] Consequently, a row of metal oxides (Al$_2$O$_3$,[16,17] V$_2$O$_5$,[18,19] ZrO$_2$,[20,21] etc.) or phosphates (AlPO$_4$,[22] Co$_3$(PO$_4$)$_2$[23]) has been employed in Ni-rich cathodes to create such protective surface coatings. In a combined approach, Sun's group designed a Ni-rich core (LiNi$_{0.8}$Co$_{0.1}$Mn$_{0.1}$O$_2$) and Mn-rich shell (LiNi$_{0.5}$Mn$_{0.5}$O$_2$) structured material with satisfactory electrochemical performance attributed to the much-improved surface stability but also to very complex synthesis conditions difficult to transfer into a larger scale.[24]

From a very different angle, Heist et al.[5] addressed this issue by employing for the first time a more stable ionic liquid electrolyte (ILE) for Ni-rich cathodes (LiNi$_{0.8}$Mn$_{0.1}$Co$_{0.1}$O$_2$) and obtained decent electrochemical performance using a bis(fluorosulfonyl) imide (FSI)-based ILE. FSI-based ILs typically display higher conductivity due to lower viscosity compared with bis(trifluoromethanesulfonyl)imide (TFSI)-based ILs but an inferior electrochemical stability toward Li-metal anodes and at elevated potentials. Herein, we followed a distinctively different approach, employing a nonflammable dual-anion ILE, allowing for stable interfaces at both Li-metal and Ni-rich electrodes. The specifically designed ILE (0.8Pyr$_{14}$FSI-0.2LiTFSI) allows for a well-balanced combination of conductivity and stability, enabling Ni-rich positive-electrode materials with very high Ni content as recently demonstrated employing lithium-rich layered cathodes.[25] Herein, this ILE is for the first time employed for nickel-rich cathode materials as a distinctive way to overcome the limitations of their electrochemical instability. The synergistic interplay of FSI$^-$ and TFSI$^-$ provides highly favorable interfacial passivation layers on the surface of both electrodes, and thereby enables dramatically improved electrochemical cycling stability through effectively mitigating material deterioration as evidenced by in-depth structural and morphological characterization in combination with a detailed analysis of the CEI formed.

[1]Helmholtz Institute Ulm (HIU), Helmholtzstrasse 11, Ulm 89081, Germany

[2]Karlsruhe Institute of Technology (KIT), P.O. Box 3640, Karlsruhe 76021, Germany

[3]Department of Solar & Energy Engineering, Cheongju University, Cheongju, Chungbuk 28503, Republic of Korea

[4]Lead contact

*Correspondence: guk-tae.kim@kit.edu (G.-T.K.), stefano.passerini@kit.edu (S.P.)

https://doi.org/10.1016/j.joule.2021.06.014
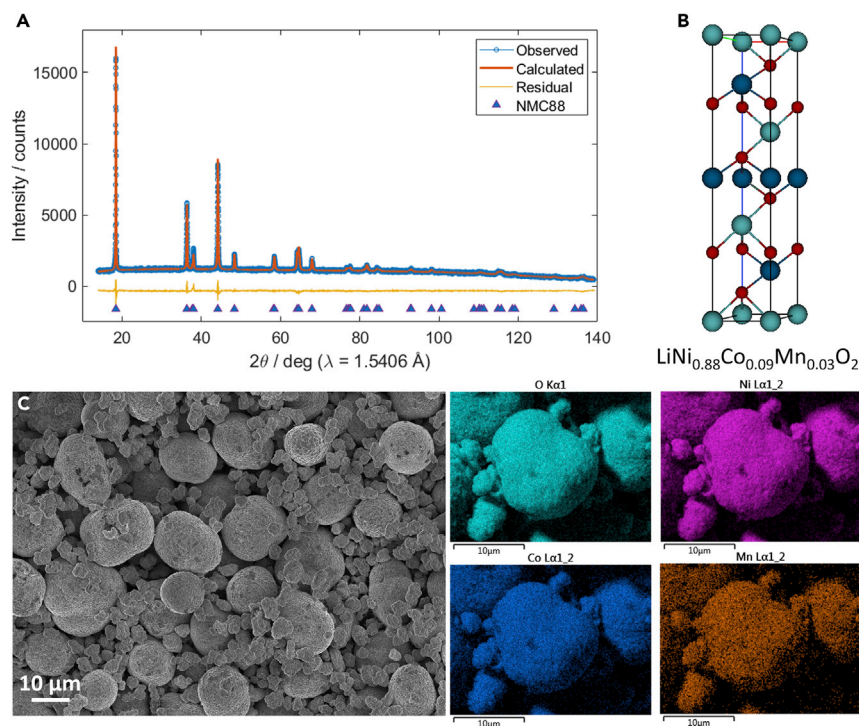
Joule
Article

CellPress
OPEN ACCESS

Figure 1. Structure and morphology of NCM88

(A) Rietveld refinement of the XRD pattern of pristine NCM88 powder.

(B) Structural model of NCM88. Red, O; light blue, interslab metal; dark blue, intralayer metal.

(C) SEM micrograph of NCM88 and its elemental mapping for oxygen (O), Nickel (Ni), Cobalt (Co), and manganese (Mn).

RESULTS AND DISCUSSION

The structural characterization of the pristine NCM88 powder together with the structural model used for the Rietveld refinement of the X-ray diffraction (XRD) pattern is reported in Figures 1A and 1B ($R_{wp} = 0.03963$; RF = 0.08328; $RF^2 = 0.13505$). NCM88 features a hexagonal layered α-NaFeO$_2$ structure[9] (space group: R-3m) with lattice parameters: a = b = 2.87280(6) Å; c = 14.1937(4) Å. The refined atomic parameters are reported in Table S1. Here, the atom labeled as "Li1" is located in the interslab layer, whereas atoms "Ni1," "Co1," and "Mn1" are in the NCM intralayer. A slight cation mixing between Li and Ni atoms was allowed by constraining the total amount of each element to 1.00 and 0.88, respectively. However, no cation mixing was detected either by letting the occupancy values float or by changing them manually, as the fit goodness did not improve. The morphology of NCM88 was characterized via scanning electron microscopy (SEM) revealing the combination of large spherical secondary particles with a diameter in a range of 10–30 μm together with smaller particles of approximately 5 μm (Figure 1C), where the secondary particles consist of numerous primary particles (Figure S1). The corresponding energy dispersive X-ray (EDX) elemental mapping demonstrates a uniform distribution of elements (Ni, Co, and Mn) over the surface of both types of NCM88 particle sizes, and the ICP-OES result confirms that the composition of the as-synthesized Ni-rich cathode material is close to the targeted stoichiometry (Table S2). For electrochemical characterization in Li||NCM88 cells, a specifically designed ILE was employed, which contains two imide-based anions.[26]

The dual-anion (0.8Pyr$_{14}$FSI-0.2LiTFSI) ILE displays excellent compatibility with Li metal as verified by galvanostatic stripping-plating in symmetrical Li/ILE/Li cells
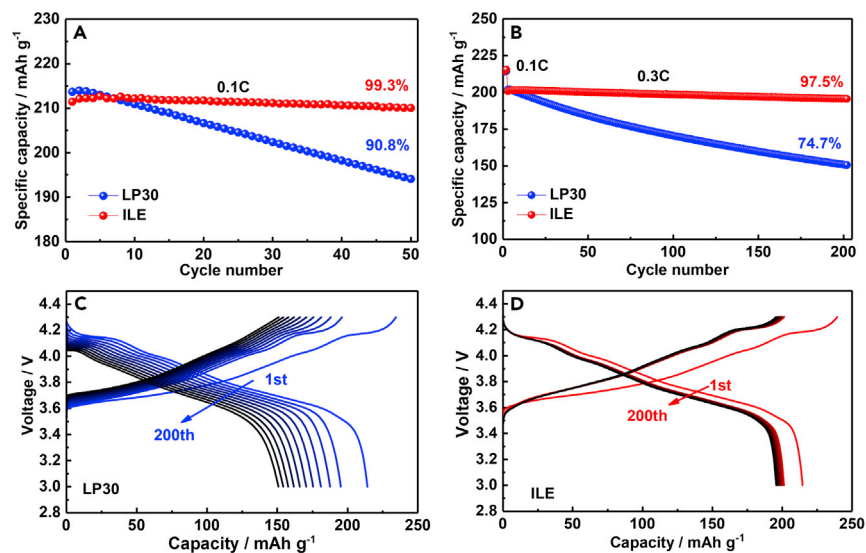
Figure 2. Electrochemical performance of Li∥NCM88 cells employing LP30 or ILE

(A–D) Galvanostatic cycling of NCM88 in LP30 (1M LiPF$_6$ in EC/DMC) and IL (0.8Pyr$_{14}$FSI-0.2LiTFSI) electrolytes at (A) 0.1C and (B) 0.3C with the corresponding selected potential profiles for the 200 cycles in (C) LP30 and (D) IL electrolyte. All two-electrode cells were tested at 20°C within the 3.0– 4.3 V cut-off voltage range.

(Figure S2), a broad electrochemical stability window (~5 V) as measured using carbon (Super C65) as working electrode at a low scan speed of 0.1 mV s^{-1} (Figure S3), as well as high ionic conductivity and rather low viscosity (Figure S4). Additionally, it allows for effective passivation of the aluminum current collector upon repeated CV scans (Figure S5). Thus, in contrast to LiTFSI-based electrolytes with organic carbonate solvents, no corrosion is observed on the Al surface (Figure S6).[27] In order to benchmark the performance of the ILE with highly Ni-rich cathodes, its performance in Li∥NCM88 cells is compared in Figure 2 with that of the conventional and commercially available organic solvent-based electrolyte (LP30, 1M LiPF$_6$ in ethylene carbonate [EC]/DMC,1:1 by volume). Both cells exhibit an initial discharge capacity greater than 210 mAh g^{-1} at 0.1C rate (1C rate corresponds to a specific current of 200 mA g^{-1}, Figure 2A). Whereas a gradual capacity decrease is apparent for the LP30 cell with a capacity retention of 90.8% after 50 cycles, the capacity retention of the ILE cell is as high as 99.3% with almost no visible capacity fade. Figure 2B compares the performance over 200 cycles at a higher specific current of 0.3C after two initial-activation cycles at 0.1C. Again, as already observed at 0.1C, an extremely stable capacity is obtained with the ILE, which shows a capacity retention of 97.5%, i.e., much higher than that of the LP30 electrolyte (74.7%). A more detailed insight into the performance difference for the two electrolytes is given by the evolution of the voltage profiles during cycling (Figures 2C and 2D). When employing LP30, it is very evident that the specific capacity as well as the average discharge voltage decay continuously and rather severely during the 200 cycles. In contrast, the performance drop is hardly noticeable when employing ILE. Only a slight capacity fade is visible in the discharge curve tail, whereas practically no voltage decay is visible from the potential profiles.

To understand the reasons for the rather different performance of NCM88 electrodes cycled in the two electrolytes (ILE and LP30), the morphology of the NCM88 particles before and after cycling was investigated (Figure 3). The low-magnification SEM images (Figures 3A–3C) show the presence of some cracks in
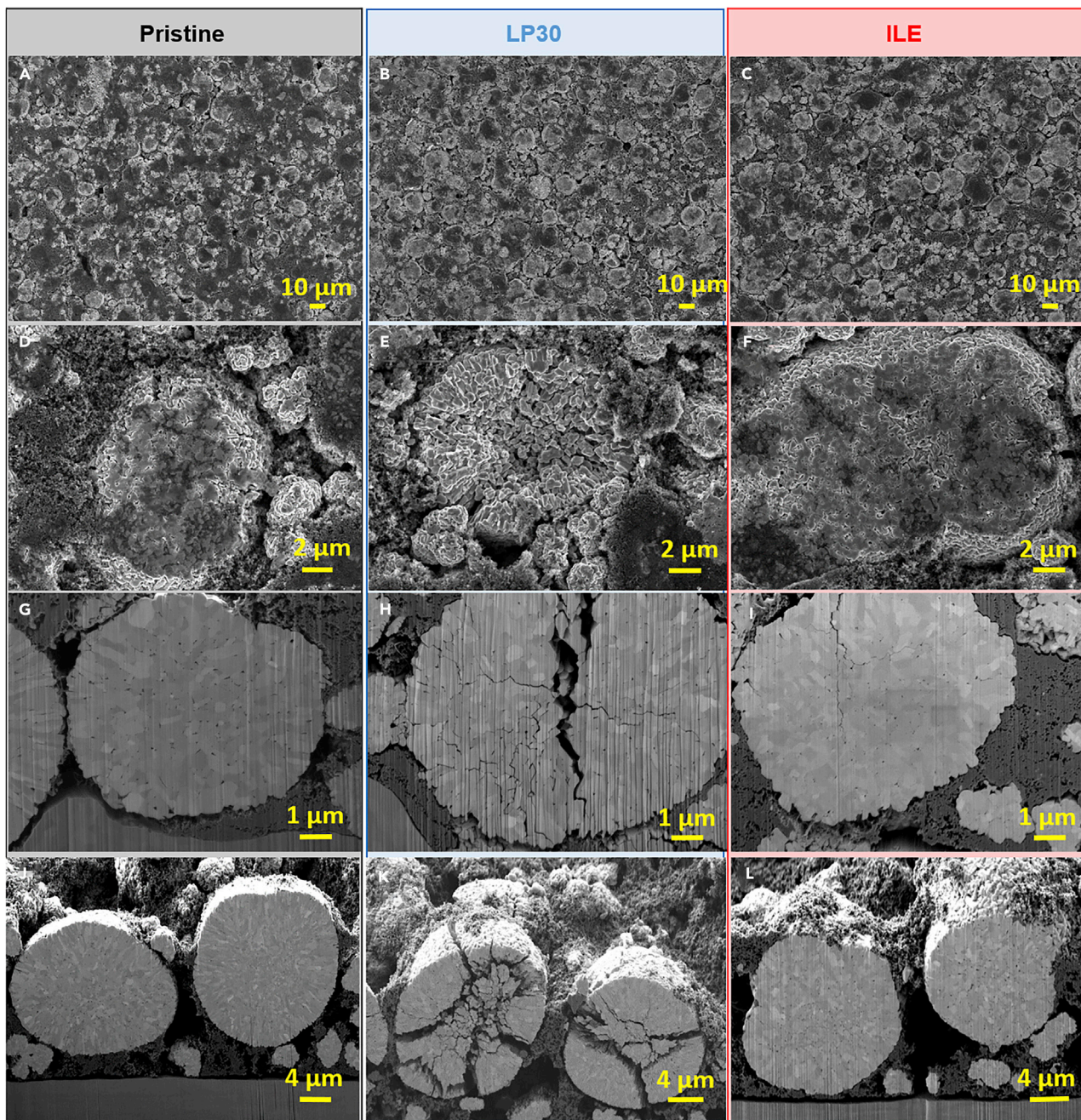
Figure 3. Morphological analysis of pristine and cycled NCM88 electrodes

(A–L) Top-view and cross-sectional SEM micrographs of pristine (fresh) NCM88 electrodes (A, D, G, and J), as well as NCM88 electrodes, after 200 cycles (at 0.3C-rate) in (B, E, H, and K) LP30 and (C, F, I, and L) ILE. The electrodes shown in (A–I) were pressed at 8 t cm^2, those shown in (J–L) are unpressed electrodes.

the coated electrodes, in particular at the particle edges, after cycling. This is expected for the electrodes swelled with electrolyte and might also occur during sample handling for microscopy preparation. However, the high-resolution micrographs clearly reveal the dramatic impact of the strain generated by the H2-H3 phase transition at high-charge state upon repeated cycling, especially in LP30. Several particles of the electrode cycled in LP30 are seriously damaged, which can be seen more

CellPress
OPEN ACCESS

Joule
Article

clearly in Figure 3E, where the secondary particles appear to be broken into several parts. In contrast, this phenomenon is not observed for the particles of the electrode cycled in ILE, which essentially appear as the fresh electrode (compare Figures 3D and 3F). In addition, the morphology of the Li-metal anodes after cycling in both electrolytes is shown in Figure S7. The surface of the Li-metal electrode cycled in LP30 presents a thick layer of mossy lithium as seen from the photographs and SEM images. In contrast, the surface of the electrode cycled in ILE appears mostly undamaged (except some lithium dendrites around the edge). Its surface appears smooth and clean, indicating that a more stable and robust solid electrolyte interphase was generated on the Li-metal surface.

In order to identify the reason for the different morphology change occurring upon cycling in the two electrolytes, the inner secondary particle morphology was investigated by acquiring SEM cross-sectional images after focused ion-beam (FIB) preparation. The fresh particle possesses a well-structured shape without any microcrack visible (Figure 3G). However, severe cracks are seen in the particle cycled in LP30 (Figure 3H) penetrating from the surface into the core along the grain boundaries of the primary particles. The vertical crack is likely caused by the mechanical stress during electrode preparation (pressing under high load), which then is amplified during repeated cycling and provides a starting point for microcrack formation offering channels for electrolyte penetration to the interior of the particle.[28] In turn, the micrograph in Figure 3I shows a much less pronounced cracking at the surface of the particle.

The origin of the microcracks was also investigated. In fact, the NCM88 electrodes are subjected to compression in order to reduce the open porosity and optimize the electronic conductivity among the particles and with the current collector. In order to verify if the formation of microcracks is merely induced by the mechanical stress during pressing, a set of non-pressed electrodes was investigated after 200 deep (dis-)charge cycles in ILE and LP30 (Figure 3J–3L). From these micrographs, it is evident that the major reason for microcrack formation in the NCM88 particles is indeed related to the cycling in LP30. In fact, the particles of the electrode cycled in ILE perfectly resemble the structure of those in the fresh electrode, showing no damage.

Overall, the combined FIB-SEM morphological investigation indicates that the superior electrochemical performance of NCM88 in ILE is associated with the reduced (if not suppressed) evolution of microcracks in the active material secondary particles resulting in a much slower active material aging in ILE. The absence of cracks implies that the electrolyte does not come in contact with the highly reactive Ni^{4+} because the CEI is not broken. Indeed, this is not the case for the electrode cycled in LP30, in which cracks develop, leading to additional degradation of the electrolyte and, suspectedly, the formation of an electrochemically inactive NiO-like rock-salt structure starting from the surface and proceeding into the core of the particles causing the pronounced performance fading and impedance increase.[29,30]

To further highlight this tremendous difference, the average-charge and -discharge voltages obtained from the voltage profiles for the two electrolytes are shown in Figure 4A. Indeed, the average-charge voltage in LP30 increased from 3.893 to 3.933 V at a rate of 0.20 mV per cycle, indicating the buildup of a resistive surface film on NCM88 upon cycling, which increases the positive-electrode polarization upon charge. This is likely associated to the formation of a resistive CEI due to parasitic reactions taking place especially at the highly delithiated state, where the presence
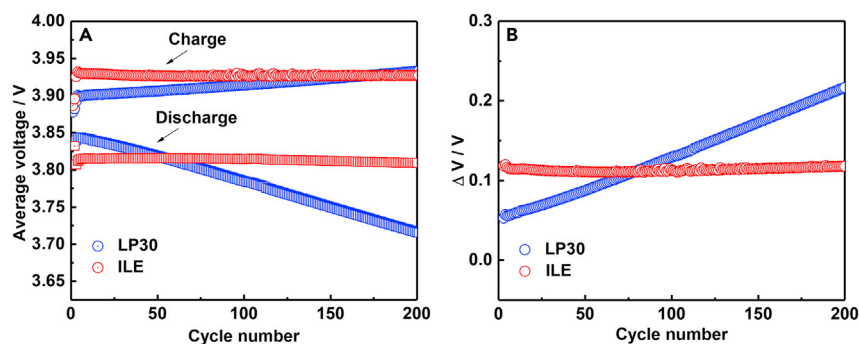
CellPress
OPEN ACCESS

Figure 4. Evolution of Li‖NCM88 cell voltage upon cycling
(A and B) (A) Average dis/charge voltage and (B) average voltage hysteresis (ΔV) of the cells upon cycling in LP30 and IL electrolyte. All two-electrode cells were tested at 20°C within the 3.0–4.3 V cut-off voltage range.

of reactive Ni^{4+} promotes severe electrolyte decomposition.[5] In addition, the evolution of microcracks inside the cathode active material particles is known to be another factor contributing to increasing cell impedance.[28,30] Although, more severely, the average discharge voltage decreased from 3.840 to 3.716 V, i.e., at a rate of 0.63 mV per cycle, which directly translates into a rapid loss of specific energy stored in the cell, which results from a serious degradation of the NCM88 crystal structure upon cycling in LP30.

In contrast, the average voltage of the NCM88 electrode during both the charge and discharge is exceptionally stable in ILE. Despite the cell polarization being initially slightly higher in the more viscous and less ion-conductive ILE, the steady lines for the average dis/charge voltage cross the de/inclining ones of LP30 making ILE the more favorable system in terms of energy-storage capability. The overall voltage hysteresis (ΔV) for the two cells, which is calculated from the difference of average-charge and -discharge voltages[31] is shown in Figure 4B. Initially, the ΔV in LP30 (0.053 V) is much lower than that in ILE (0.118 V). However, it continuously increases to 0.217 V after 200 cycles. In contrast, ΔV resembles a steady line upon long-term cycling in ILE, indicating that a less resistive and highly stable CEI is formed in this electrolyte and suggests an undamaged NCM88 structure.

In order to further highlight the capacity and voltage fade differences occurring in the NCM positive electrodes cycled in the two electrolytes (ILE and LP30), the differential-capacity curves are compared in Figure 5. Each distinct peak in the differential-capacity curves corresponds to a specific phase transition, i.e., hexagonal H1 to monoclinic M to hexagonal H2 to hexagonal H3, during lithium insertion/extraction.[32] It is important to notice that the phase transformation from H2 to H3 at high-charge state is accompanied by a highly anisotropic lattice strain,[28,32] which may strongly affect the structural stability of the NCM88 particles. As a matter of the fact, a dramatic decrease of the H2-H3 peak is observed upon cycling in LP30 (Figure 5A), which indicates a poor reversibility of the H2-H3 phase transition in such an electrolyte. This becomes even more evident in the plot of the normalized integrated peak intensity versus cycle number as shown in Figure 5B. Over 200 cycles, the gradual decrease of the differential-capacity peak translates into a reduction of 33.2%, indicating this partially irreversible phase transformation as the strongest contribution to the NCM88 capacity fading. However, the differential-capacity curves for the NCM88 electrode cycled in ILE practically overlap over the 200 cycles indicating a highly reversible H2-H3 phase transformation to occur in this
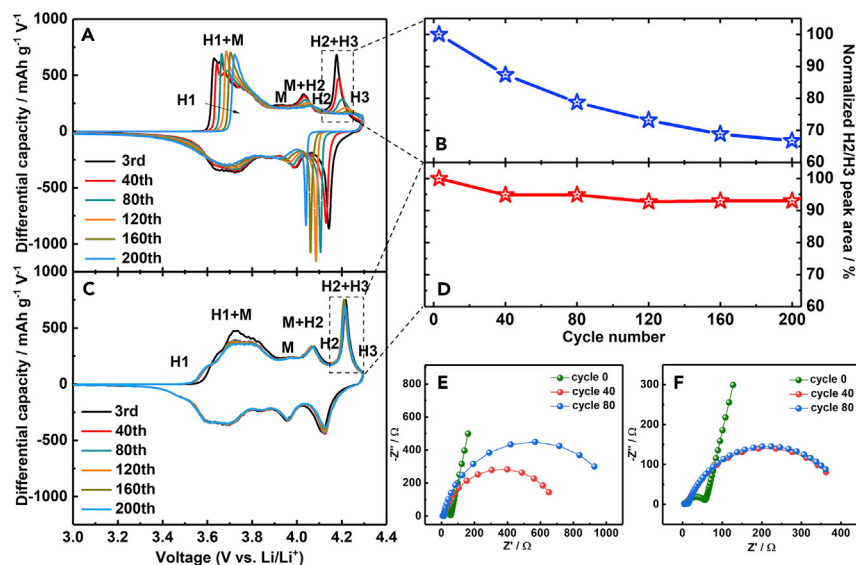
Figure 5. Correlation between structural (in)stability of NCM88 and electrochemical performance of Li∥NCM88 cells in the two electrolytes

Comparison of Li/NCM88 cell employing in LP30 and ILE upon 200 galvanostatic cycles at 0.3C (20°C, 3.0–4.3 V).

(A and B) (A) Differential-capacity plots for selected cycles using LP30 electrolyte and (B) evolution of the peak area corresponding to the H2/H3 phase transition.

(C and D) The same analysis for the ILE is given in (C) and (D).

(E and F) Evolution of the EIS response before cycling and during cycling of the same electrodes in (E) LP30 and (F) ILE.

electrolyte.[30] In fact, Figure 5D reveals only a 7.0% reduction of the H2-H3 peak after 200 cycles. The dQ/dV peak for the reverse phase transformation (H3-H2) is observed during the discharge process. It remains essentially unchanged for the electrode cycled in ILE, but it is strongly affected for that cycled in LP30. Therefore, the severe performance fading occurring in LP30 electrolyte is certainly associated to the partial irreversibility of the H2-H3 phase transformation finally leading to the incremental formation of microcracks at the grain boundaries of the primary NCM88 particles. The growth of such microcracks would result in an increasing resistance of the cell, which is well supported by the electrochemical impedance spectroscopy (EIS) data collected upon cycling (Figures 5E and 5F) that show a concomitant increase of the cell resistance. A preliminary (qualitative) analysis of these data clearly illustrates a largely increasing charge-transfer resistance for the NCM88 electrode cycled in LP30 during the initial 80 cycles, i.e., where the H2-H3 peak intensity drops most severely. Although before cycling the ILE cell has a higher charge-transfer impedance compared with the LP30 one; it stays steady upon 80 cycles becoming lower than that of the cell employing LP30 as the electrolyte. Again, this points toward a more stable interface formed between the ILE and NCM88 as well as a lower degradation of the latter material, which remains intact upon cycling and is not broken by the formation of microcracks within the secondary particles.

To relate the formation of microcracks to the structural changes of the NCM88 particles upon cycling, an in-depth *in situ* XRD study was performed (Figure 6). The voltage profiles during the first-charge process in LP30 and ILE are presented alongside the evolution of the (003) and (104) reflections of NCM88 in Figures 6A and 6B. In fact, the (003) feature is the most pronounced for NCM88, allowing it to easily follow the change occurring along the *c*-lattice parameter of space group R-3m,
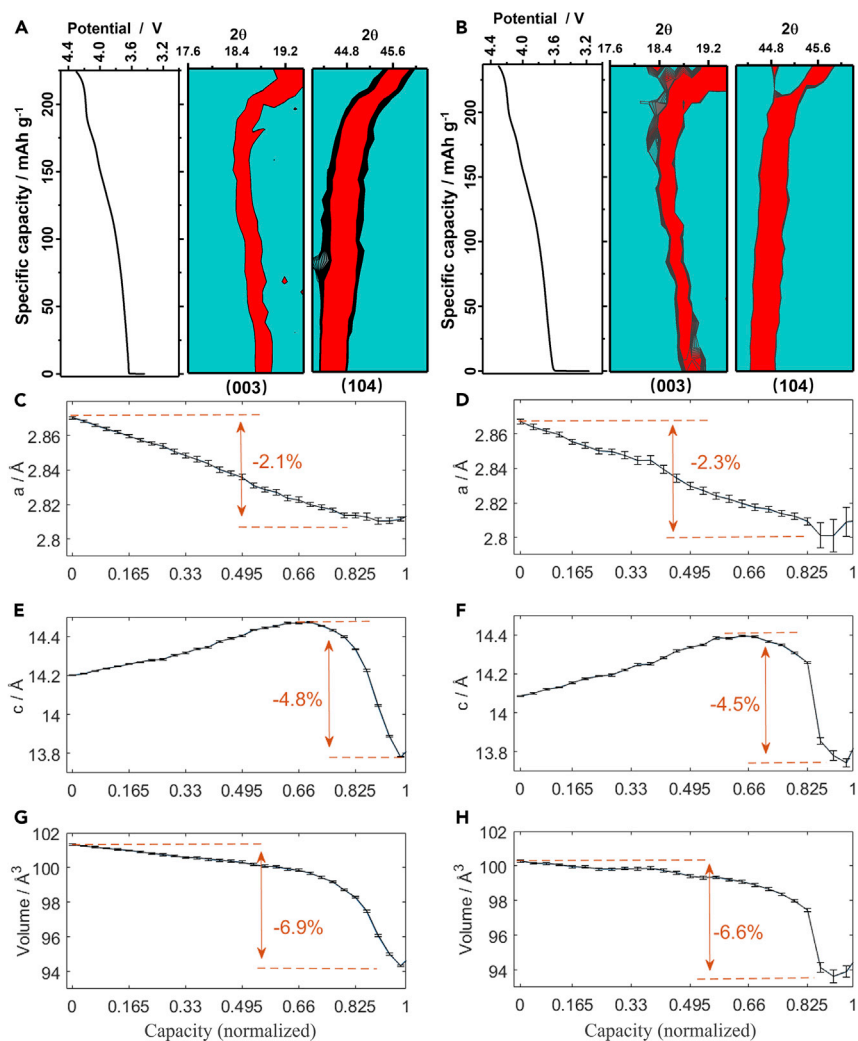
Joule
Article

CellPress
OPEN ACCESS

Figure 6. Structural strain of NCM88 upon initial galvanostatic cycling

(A–H) Variation of the lattice parameters and the unit cell volume of NCM88 during the first-charge process in LP30 (A, C, E, and G) and ILE (B, D, F, and H).

whereas the (104) feature is characteristic of both the layered and rock-salt NiO structure.[33] Moreover, the I_{003}/I_{104} ratio is a useful indication to evaluate cation mixing in layered oxide materials. For both electrolytes the (003) reflection shifts to slightly lower angles during the charge process from open circuit voltage (OCV) to ~ 4.1 V before it dramatically shifts in the reverse direction, i.e., to higher angles in the range of $4.1 \sim 4.3$ V. This indicates a much narrower interlayer distance, which is caused by the extraction of most of the Li$^+$ from the lithium layer. The (104) reflection displays a similar behavior at the high state of charge, i.e., sudden lattice contraction upon deep delithiation. Although, differently to the (003) reflection, this reflection shows a continuous shift toward higher and lower angles at the beginning and end of the charge/discharge cycle, respectively. When comparing the NCM88 in the two electrolytes, there is no apparent difference. However, the extent of the overall shift for ILE is slightly smaller than that in LP30. In order to work out this difference in more detail, the lattice parameters a and c and the unit cell volume V were calculated from the Rietveld refinement of the whole *in situ* XRD datasets. The results are summarized in Figures 6C–6H for the entire charge process of

Joule
Article

NCM88 in LP30 and ILE. In accordance with the (104) reflection shift, the lattice parameter *a* experiences a monotonous decrease during charge in both cases. The overall *a* contraction (Δ*a*) during the full charge process remains relatively low, i.e., below 2.5%. However, the *c*-lattice value shows a more complicated trend as it is also observed for the shift of the (003) reflection. Initially, the *c* value gradually increases but experiences a sudden contraction when the H2-H3 phase transformation occurs at high state of charge. Previously (see Figure 5), it was found that the (H2-H3) phase transition process becomes increasingly irreversible over cycling in the LP30 electrolyte, thus, remaining to some extent in the unfavorably strained H3 phase. This is reflected in the absolute degree of c-axis contraction (Δ*c*), which is larger in LP30 (4.8%) than the 4.5% in ILE. The reason for the lower c-axis contraction in ILE can probably be attributed to a more robust CEI layer protecting the electrolyte against the reactivity of Ni^{4+} in the highly delithiated state, alleviating Li^+/Ni^{2+} cation mixing and structural decay. Obviously, the abrupt and more pronounced contraction along the c axis induces severe mechanical strain, which directly translates into an overall larger change of the unit cell volume (Δ*v*) comparing LP30 and ILE (6.9% versus 6.6%). Eventually this difference results in the formation of microcracks at grain boundaries and finally, destroys the secondary particles,[28] as can be seen on the SEM micrographs of NCM88 particles cycled in LP30.

As both issues, irreversible phase transformation and microcrack formation are typically penetrating from the particles' surface into their core, the origin of the dramatically improved performance and lower (crystal) volume change in IL is most probably related to the interaction of the electrolyte with the active material particle surface. Therefore, we investigated the composition of the CEI layers formed on the electrodes cycled in each electrolyte by means of X-ray photoelectron spectroscopy (XPS, Figure 7). In addition to the outermost surface layer of the CEI, measurements were also carried out after removing ~3 nm of the topmost surface material (by 30 min of Ar^+ sputtering) to gain insight into the depth distribution of the different species. The XPS spectra of NCM88 electrodes cycled in LP30 are shown in Figure 7A. The detail spectrum in the C1s region contains four peaks at 284.8, 286.3, 288.6, and 290.8 eV. The first signal (at 284.8 eV) can be attributed to C-C/C-H species and includes contributions from the conductive carbon (Super C65) and CH_x functionalities that are formed upon decomposition of EC and dimethyl carbonate (DMC) during cycling. The second feature (at 286.3 eV) comprises C–O species, e.g., from polyethylene oxide (PEO)-like species formed by EC polymerization,[34] and the CH_2 groups of PVdF, which are shifted to high binding energy by the neighboring CF_2 groups. The C=O/O–C=O groups associated, e.g., to lithium alkyl carbonates ($ROCO_2Li$) from decomposition of DMC, or to remaining impurities of carbonates on the surface of the NCM88 powder after synthesis and storage (Figure S8), are associated to the peak at 288.6 eV, whereas the feature at 290.8 eV is caused by the CF_2 groups of PVdF. Matching the C 1s features, signals due to C=O/O–C=O (531.6 eV) and C–O (533.5 eV) species are also observed in the spectra in the O 1s region. In addition, a peak due to the oxygen in the active material is also observed at 529.4 eV. In the F 1s spectra peaks due to LiF (685.0 eV), $LiPF_6/Li_xPO_yF_z$ (686.8 eV), and the CF_2 groups of PVdF (687.8 eV) are detected. Finally, the P 2p region shows peak doublets due to undecomposed $LiPF_6$ (P $2p_{3/2}$ peak at 136.4 eV) and of $Li_xPO_yF_z$ species (P $2p_{3/2}$ peak at 134.2 eV). Furthermore, the measurements after sputtering demonstrate an increase of the decomposition products (both $Li_xPO_yF_z$ and LiF). This result indicates extensive decomposition of the electrolyte salt, $LiPF_6$.[34] Such a decomposition, occurring under self-catalytic conditions, is accompanied by the formation of HF, which is highly detrimental for
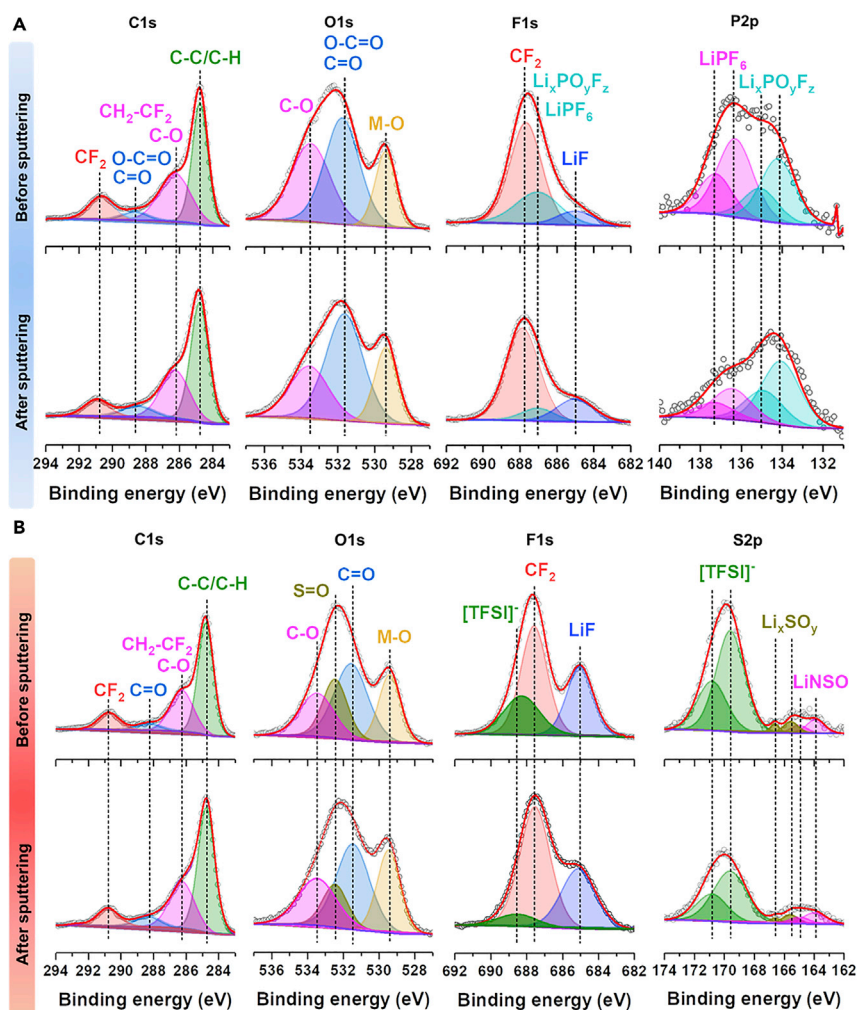
Figure 7. Characterization of the CEI on NCM88 after cycling
(A and B) XPS analysis of NCM88 electrodes after 200 cycles in (A) LP30 and (B) IL electrolyte recorded before (top) and after (bottom) Ar$^+$-sputtering.

the positive-electrode material.[25] In fact, HF attacks the NCM particles, accelerating the Li$^+$/Ni^{2+} cation mixing and promoting the formation of rock-salt phase (NiO-like) impurity regions, especially near the surface.[5]

The spectra of the NCM88 electrodes cycled in ILE (Figure 7B) display some distinct differences. First, additional features appear in the O1s region (peak at 532.4 eV due to the O=S=O group), which are clearly associated to the presence of LiTFSI and its decomposition products in the CEI. Second, and more importantly, the F 1s spectrum clearly displays a higher LiF peak (685.0 eV) than that observed for the NCM88 electrode cycled in LP30 in spite of the absence of LiPF$_6$ in ILE. It deserves to be noted that a larger fraction of LiF in the CEI is rather important since LiF is a key component for the stability of the CEI. The LiF formation mechanism in ILE involves the S–F bond cleavage of FSI$^-$[35] substantially differing from that of LiPF$_6$ in organic solvent-based electrolytes where the concomitant generation of HF occurs.[36,37] Additionally, the CEI formed in ILE contains S-containing species, e.g., Li$_x$SO$_y$ and LiNSO are identified in the S2p region, which have a beneficial influence on its stability[25] because of their electronically insulating and ion conducting properties.
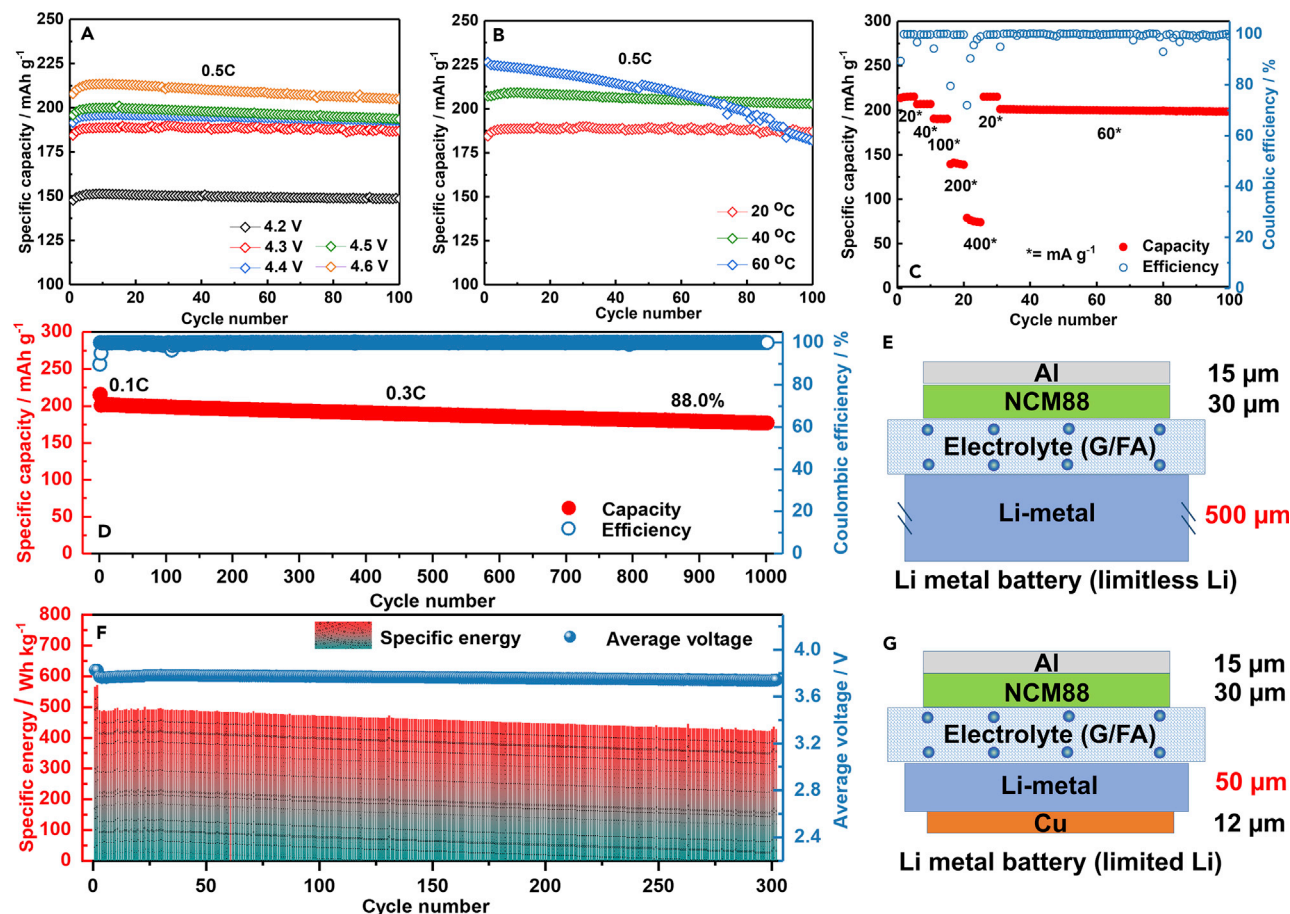
Figure 8. Practical assessment of Li|ILE|NCM88 cells: Effect of cut-off voltage, temperature, and Li-foil thickness on the electrochemical performance

(A and B) Galvanostatic cycling of Li/ILE/NCM88 cells at (A) different cut-off voltage (20°C) and (B) different temperature in ILE (3.0–4.3 V).

(C–E) (C) Rate capability test and (D) long-term cycling performance of an exemplary Li/ILE/NCM88 cell employing a thick Li-metal (500 μm) anode (20°C, 3.0–4.3 V) according to the scheme in (E).

(F and G) (F) Specific energy and average discharge voltage evolution of the Li/ILE/NCM88 cell with a thin Li-metal (50 μm) anode (initial two cycles at 0.1C, following cycles at 0.5C, 20°C, 3.0–4.3V) according to scheme (G). The Coulombic efficiency in (D) is also reported in a magnified scale in Figure S12.

Overall, the avoidance of HF formation as well as the presence of LiF and S-containing inorganic salts are probably the reason for the highly stable electrochemical performance of NCM88 in ILE.

After clarifying the reasons for the extremely stable cycling behavior of NCM88 in ILE, the performance of Li|ILE|NCM88 cells was assessed toward their practical application via a series of different electrochemical measurements (Figure 8). First of all, the long-term performance of NCM88 upon galvanostatic cycling was evaluated toward increasing upper cut-off voltage. This is an important parameter as the cell energy density increases with the upper cut-off voltage since it results in the increase of the NCM88 specific capacity. As seen in Figure 8A, the cut-off voltage of 4.2 V results in a very stable delivered capacity, but the discharge capacity is rather low since the H2-H3 phase transition, occurring in the 4.2–4.3 V range, see Figure S9) is not accessed. Upon increasing upper cut-off voltages higher specific capacities are obtained (see Figure 8A); however, the excessive Li$^+$ extraction from the NCM88 material leads to the irreversible multiphase transition eventually resulting in the formation of NiO_2. This accelerates the generation of stacking faults and severely

compromises structural stability as shown by the decreasing capacities upon long-term cycling (Figure 8A) at the highest upper cut-off voltages.[33] In Table S3 the specific first-charge capacity and the capacity retention upon cycling of LiIILEINCM88 cells are summarized for a few selected upper cut-off voltages. The values clearly show the upper cut-off of 4.3 V represents best compromise between energy-storage capacity and cycle life of the cell.

Following, the effect of temperature on the cell performance was evaluated while keeping the upper cut-off voltage fixed to 4.3 V. Figure 8B reveals very stable cycling of NCM88 in ILE at 20°C, where practically no fading of the capacity can be observed. At 40°C, the ILE's viscosity decreases and the ionic conductivity increases, resulting in the specific capacity increasing by around 20 mAh g^{-1}, but with the onset of a slightly decreasing trend over cycling. Finally, at 60°C, the cell displays a pronounced fading, which is expected from the poor thermal stability of Ni-rich cathode materials.[38] The rate capability assessment of the LiIILEINCM88 cells was conducted in the range from 20 to 400 mA g^{-1} (Figure 8C). The result shows that the NCM88 can deliver appreciably high specific discharge capacities in ILE, when relatively low currents are applied, i.e., 214 mAh g^{-1} @ 20 mA g^{-1}, 207 mAh g^{-1} @ 40 mA g^{-1}, and 190 mAh g^{-1} @ 100 mA g^{-1}. However, at higher currents the specific capacity drops notably (139 mAh g^{-1} @ 200 mA g^{-1}, 79 mAh g^{-1} @ 400 mA g^{-1}). The lower performance of NCM88 in ILE with respect to LP30 (213 mAh g^{-1} @ 20 mA g^{-1}, 204 mAh g^{-1} @ 40 mA g^{-1}, 191 mAh g^{-1} @ 100 mA g^{-1}, 180 mAh g^{-1} @ 200 mA g^{-1}, 168 mAh g^{-1} @ 400 mA g^{-1}, see Figure S10) is associated to the higher viscosity of ILE at 20°C compared with commercial organic carbonate-based electrolytes. However, this slightly lower performance is very well compensated by the substantially lower fading at 20°C and, even more, at 40°C (see Figure S11).

Last, but not least, it is important to notice the long-term stable cycling of the Li/ ILE/NCM88 cells without the formation short-circuits. In this regard, the presented ILE demonstrates an outstanding stability with a capacity retention of 88.0% after 1,000 deep (dis)charge cycles at 0.3C and 20°C (Figure 8D). Such a capacity retention upon long-term cycling of LiIILEINCM88 cells corresponds to an irreversible capacity loss of only 0.024 mAh g^{-1} per cycle with an average Coulombic efficiency around 99.94% (Figure S12). Even more interestingly, the working voltage is exceptionally stable in terms of average discharge voltage that only drops by 0.037 V over the full 1,000 cycles (3.67×10^{-5} V per cycle). These cells, made accordingly to the design shown in Figure 8E, achieved very high specific energies, i.e., 822 Wh kg$_{NCM}^{-1}$ at 0.1C, and 764 Wh kg$_{NCM}^{-1}$ at 0.3C (Figure S13). In order to evaluate the specific energy from an industrial perspective, cells employing a much thinner Li-metal foil (50 µm) were realized as shown in Figure 8G. These lab-scale cells show a remarkable stability upon cycling achieving a capacity retention of 88.3% after 300 cycles (Figure S14). The resulting specific energy based on the overall (anode + cathode) active material weights is calculated to be 564 Wh kg^{-1} at 0.1C, and 488 Wh kg^{-1} at 0.5C using the thin Li electrode. Furthermore, to demonstrate the practical relevance of such NCM88IILEILi-metal cells we have carried out preliminary measurements using high areal loading NCM88 electrodes (~9 mg cm^{-2}) with an increased areal capacity (~1.9 mAh cm^{-2}). Despite the high loading we achieved excellent electrochemical performance using the ILE as shown in Figure S15. To the best of our knowledge, the LiIILEINCM88 lab-scale cells herein realized offer the best long-term cycling performance achieved with Li-metal anode and nickel-rich cathode materials, significantly pushing forward the state of the art in high-energy lithium batteries with liquid electrolytes.

Conclusion

In this work, we demonstrated an effective approach to dramatically enhance the electrochemical as well as structural stability of nickel-rich positive-electrode materials (i.e., $LiNi_{0.88}Co_{0.09}Mn_{0.03}O_2$). Through harnessing the synergistic interplay of the complementary FSI^- and $TFSI^-$ salts employed in a low-volatility and non-flammable dual-anion ILE ($0.8Pyr_{14}FSI-0.2LiTFSI$) allowed for ultra-stable long-term cycling of NCM88|ILE|Li-metal cells with an outstanding capacity retention of 88% over 1,000 cycles, with practically zero voltage decay (3.67×10^{-5} V per cycle) and excellent Coulombic efficiency above 99.94%. The use of a limited thin-film (50 μm) Li-metal anode leads to a superior specific energy of 564 Wh kg^{-1} exceeding the state of the art of Li-metal cells with liquid electrolyte. The origin of this great improvement is found in the exceptionally stable CEI layer formed in ILE. This layer protects the NCM88 surface against detrimental reactions with the electrolyte and therefore prevents the irreversible phase transformation of the hexagonal lattice at the crystal surface and avoids the formation of microcracks penetrating into the secondary particle architecture.

EXPERIMENTAL PROCEDURES

Resource availability

Lead contact

Further information and requests for resources and materials should be directed to and will be fulfilled by the lead contact, Stefano Passerini (stefano.passerini@kit.edu).

Materials availability

The materials in this study will be made available upon reasonable request.

Data and code availability

The datasets generated in this study are available from the lead contact on reasonable request.

Sample preparation

The ILE ($0.8Pyr_{14}FSI-0.2LiTFSI$) was prepared by dissolving LiTFSI (battery grade, 99.5 wt %, 3M) in $Pyr_{14}FSI$ in a molar ratio of 2:8. The neat ionic liquid was pre-dried at 80°C in a tubular vacuum oven (Büchi), remaining volatile compounds were then removed at RT by a turbo molecular pump ($p < 10^{-7}$ mbar). The commercially available electrolyte (LP30, Selectilyte, BASF), consisting of 1M $LiPF_6$ in a mixture of EC and dimethyl carbonate (DMC) (1:1 by volume) was chosen for comparison, the water content is below 15 ppm. The NCM88 electrodes were prepared by mixing the active material, conductive carbon Super C65 (IMERYS), and polyvinylidene difluoride binder (PVdF, Solef 6020, Solvay) in a weight ratio of 92:4:4. A slurry (solid content > 60%) was prepared using *N*-methyl-2-pyrrolidone (NMP; anhydrous, > 99.5%; Sigma-Aldrich) as dispersant and solvent, which was cast onto an aluminum foil (15 μm). After drying in the dry room overnight, the electrodes were punched into disks of 12 mm diameter and vacuum dried at 120°C for 12 h. Finally, they were pressed at 8 ton cm^{-2} (except differently specified). The average areal loading was around 2.8 $\pm$ 0.3 mg cm^{-2}, but preliminary tests on high areal loading (9 mg cm^{-2}) were also performed. Finally, the porosity of the pressed electrodes was ~30%. The lithium-coated copper foil (thickness of Li: 50 μm on 12 μm Cu) was punched into disks of 12 mm diameter.

Electrochemical measurements

The electrochemical performance of Li-metal cells employing LP30 for galvanostatic cycling was evaluated in coin cells (CR2032) assembled in an argon-filled glove box

Joule
Article

CellPress
OPEN ACCESS

(O_2 < 0.1 ppm, H_2O < 0.1 ppm) using Whatman glass fiber sheets (GF/D) as separator and lithium-metal disks as counter electrode. All other electrochemical characterization was conducted in pouch cells (using GF/A Whatman glass fiber sheets), which were assembled in the dry room (dew point < −60°C). Galvanostatic cycling was performed in a Maccor battery tester 4300. NCM88 electrodes were cycled within 3.0 and 4.3 V at 0.1C during the first two (formation) cycles and then at 0.3C. All potential values refer to the Li/Li$^+$ quasi-reference redox couple. The anodic electrochemical stability of $0.8Pyr_{14}FSI$-$0.2LiTFSI$ electrolyte was evaluated by linear sweep voltammetry (Solartron 1260) using carbon (Super C65, Imerys, supported on Al foils) working electrodes and Li metal as counter electrode. The cell voltage was swept at 0.1 mV s^{-1} from the OCV toward more positive (anodic) or negative (cathodic) voltages. The aluminum dissolution was tested by cyclic voltammetry using aluminum as working electrode at the scan rate of 0.1 mV s^{-1} in $0.8Pyr_{14}FSI$-$0.2LiTFSI$. EIS of Li-metal cells was performed using a VMP multichannel potentiostat (Bio-Logic). Impedance spectra were collected from the cells in the fully discharged state every 20 galvanostatic (dis)charge cycles within the 1–10 MHz frequency range by applying a 5-mV voltage amplitude. The (dis)charge rate of 1C corresponds to a specific current of 200 mA g^{-1}. Except specific samples, all electrochemical measurements were performed in climatic chambers set at 20°C $\pm$ 2°C.

Materials characterization

The morphology and structure of samples was investigated by SEM (ZEISS Crossbeam XB340 equipped with an EDX detector). To investigate the internal structure of the electrode and active material particles, cross-sections were prepared on a Capella FIB (gallium ion source) system using milling and polishing currents of 30 and 3 nA at an acceleration voltage of 30 kV, respectively. All samples recovered from cycled cells were transferred to the microscope under argon atmosphere using an air-tight transfer box (Sample Transfer Shuttle, SEMILAB). Micrographs were acquired from the top and in cross-sectional configuration (under a tilt-angle of 54°) after FIB preparation using smart SEM software for tilt correction to compensate for the image distortion due to the tilt of 54° to the optical axis. XPS was conducted on a Specs XPS system with a Phoibos 150 energy analyzer using monochromatic Al K$_\alpha$ radiation (1,486.6 eV), a take-off angle of 45° and pass energies of 30 and 90 eV at the analyzer for detail and survey spectra, respectively. For sample preparation, the cycled electrodes were thoroughly washed with DMC, dried, and transferred under inert gas to the XPS system. The samples were either investigated directly or after Ar$^+$ ion sputtering for 30 min (~0.1 nm min^{-1} sputter rate, 0.03 μA, 5 kV). Casa XPS was used for data analysis, using Shirley-type backgrounds and Gaussian-Lorentzian peak shapes. For the p peaks (P2p and S2p), peak doublets with the expected intensity ratio (2:1) and spin-orbit splitting(s) were used in the fit. All XPS spectra were calibrated to the C (1s) peak of conductive C additive / adventitious C (C–C/C–H species) at 284.8 eV.

The conductivity of the ILE was measured by a conductometer equipped with a frequency analyzer and a thermostatic bath (MMates Italia). The electrolyte was sealed in glass conductivity cells (assembled in the glove box) equipped with two platinized-platinum electrodes. The cell constant was determined using a 0.01 M KCl standard solution. The measurements were performed in the temperature range from −30°C to 80°C and recorded every 5°C. The equilibration time at each temperature was set to 1 h. The viscosity measurement was performed in the dry room using an Anton-Paar Physica MCR301 rheometer in cone-plate geometry.

XRD patterns were recorded by means of a Bruker D8 diffractometer equipped with a Cu Kα source (λ = 0.15406 nm) in the 10° < 2θ < 140° range with a step size of

0.010° and a 1.4 s/point acquisition time for the powder sample, whereas the *in situ* datasets were acquired in the 10° < 2θ < 88.5° range with a step size of 0.022° and a 0.5 s/point acquisition time.

Operando XRD experiments were performed using a test cell (ECC-Opto-Std, EL cell) with a polyimide window on a Bruker D8 Advance diffractometer (Cu K$_\alpha$ radiation, λ = 0.154 nm) in the 2θ range between 10° ≤ 2θ ≤ 90°. During slow charge (15 mA g^{-1} for LP30, 18 mA g^{-1} for IL) to 4.3 V, XRD patterns were continuously recorded every 30 min. For these tests, the cathode electrodes were prepared casting the electrode slurry (active material, Super C65 and PVdF in a weight ratio of 85:10:5) on aluminum mesh (16 mm). The electrodes were stored in the dry room overnight, then further dried under dynamic vacuum at 120°C for 12 h.

Rietveld refinement of the powder was conducted in the 14° < 2θ < 140° range using GSAS-II software.[39] The structural model reported by the Zheng et al.[40] was modified according to the actual stoichiometry of the NCM88 material, i.e., by considering a fixed elemental composition ratio of Ni:Mn:Co = 88:3:9. The background was fitted with a Chebyshev polynomial function with six coefficients. The instrumental parameters were obtained from a LaB$_6$ standard; accordingly, the instrumental broadening parameters, i.e., U, V, W, X, and Y, were kept fixed to $4.397 \cdot 10^{-4}$ deg^2, $-5.720 \cdot 10^{-4}$ deg^2, $2.577 \cdot 10^{-4}$ deg^2, $1.855 \cdot 10^{-2}$ deg, and $2 \cdot 10^{-5}$ deg, respectively. The peak shape was refined with a generalized micro strain broadening model and by optimizing the respective parameters, calculated as unitless fraction of $\Delta d/d \cdot 10^6$ (being *d* the interplanar distance) and due only to the sample. The scale, background, sample displacement, unit cell parameters, peak shape, and atomic parameters were refined in this order.

Sequential Rietveld refinement of the *in situ* datasets was performed in the 17.5° < 2θ < 88.5° range, by considering as the structural model the one obtained for the NCM88 powder (see above) and by fixing the atomic parameters. The background was fitted by taking into account the XRD pattern of a polyimide window (which served as transparent window in the *in situ* XRD measurements) and by adding six coefficients to a Chebyshev polynomial function. The instrumental parameters were kept fixed as for the powder, whereas the peak shape was refined by optimizing the isotropic micro strain model parameter. The scale, background, unit cell parameters, and peak shape were refined in this order.

SUPPLEMENTAL INFORMATION

Supplemental information can be found online at https://doi.org/10.1016/j.joule.2021.06.014.

ACKNOWLEDGMENTS

AUTHOR CONTRIBUTIONS

F.W. performed the (*in situ*) XRD characterization and electrochemical measurements with the support of S.F. and drafted the manuscript. M.K. performed the

Joule
Article

CellPress
OPEN ACCESS

REFERENCES

1. Li, W., Erickson, E.M., and Manthiram, A. (2020). High-nickel layered oxide cathodes for lithium-based automotive batteries. Nat. Energy 5, 26–34. https://doi.org/10.1038/s41560-019-0513-0.

2. Liu, W., Oh, P., Liu, X., Lee, M.J., Cho, W., Chae, S., Kim, Y., and Cho, J. (2015). Nickel-rich layered lithium transition-metal oxide for high-energy lithium-ion batteries. Angew. Chem. Int. Ed. Engl. 54, 4440–4457. https://doi.org/10.1002/anie.201409262.

3. Vaalma, C., Buchholz, D., Weil, M., and Passerini, S. (2018). A cost and resource analysis of sodium-ion batteries. Nat. Rev. Mater. 3, 18013. https://doi.org/10.1038/natrevmats.2018.13.

4. Sun, Y.-K. (2019). High-capacity layered cathodes for next-generation electric vehicles. ACS Energy Lett. 4, 1042–1044. https://doi.org/10.1021/acsenergylett.9b00652.

5. Heist, A., Hafner, S., and Lee, S.-H. (2019). High-energy nickel-rich layered cathode stabilized by ionic liquid electrolyte. J. Electrochem. Soc. 166, A873–A879. https://doi.org/10.1149/2.0071906jes.

6. Huang, Z., Gao, J., He, X., Li, J., and Jiang, C. (2012). Well-ordered spherical LiNixCo(1−2x)MnxO2 cathode materials synthesized from cobolt concentration-gradient precursors. J. Power Sources 202, 284–290. https://doi.org/10.1016/j.jpowsour.2011.10.143.

7. Kang, K., and Ceder, G. (2006). Factors that affect Li mobility in layered lithium transition metal oxides. Phys. Rev. B 74. https://doi.org/10.1103/PhysRevB.74.094105.

8. Zhang, S.S. (2020). Problems and their origins of Ni-rich layered oxide cathode materials. Energy Storage Mater. 24, 247–254. https://doi.org/10.1016/j.ensm.2019.08.013.

9. Wu, F., Kim, G.T., Kuenzel, M., Zhang, H., Asenbauer, J., Geiger, D., Kaiser, U., and Passerini, S. (2019). Elucidating the effect of iron doping on the electrochemical performance of cobalt-free lithium-rich layered cathode materials. Adv. Energy Mater. 9, 1902445. https://doi.org/10.1002/aenm.201902445.

10. Xie, Q., Li, W., and Manthiram, A. (2019). A Mg-doped high-nickel layered oxide cathode enabling safer, high-energy-density Li-ion batteries. Chem. Mater. 31, 938–946. https://doi.org/10.1021/acs.chemmater.8b03900.

11. Chen, M., Zhao, E., Chen, D., Wu, M., Han, S., Huang, Q., Yang, L., Xiao, X., and Hu, Z. (2017). Decreasing Li/Ni disorder and improving the electrochemical performances of Ni-rich LiNi0.8Co0.1Mn0.1O2 by Ca Doping. Inorg. Chem. 56, 8355–8362. https://doi.org/10.1021/acs.inorgchem.7b01035.

12. Li, Y.-C., Xiang, W., Wu, Z.-G., Xu, C.-L., Xu, Y.-D., Xiao, Y., Yang, Z.-G., Wu, C.-J., Lv, G.-P., and Guo, X.-D. (2018). Construction of homogeneously Al3+ doped Ni rich Ni-Co-Mn cathode with high stable cycling performance and storage stability via scalable continuous precipitation. Electrochim. Acta 291, 84–94. https://doi.org/10.1016/j.electacta.2018.08.124.

13. Song, M.Y., Lee, D.S., and Park, H.R. (2012). Electrochemical properties of LiNi1−yTiyO2 and LiNi0.975M0.025O2 (M=Zn, Al, and Ti) synthesized by the solid-state reaction method. Materials Research Bulletin 47, 1021–1027. https://doi.org/10.1016/j.materresbull.2012.01.003.

14. Yang, H., Wu, H.H., Ge, M., Li, L., Yuan, Y., Yao, Q., Chen, J., Xia, L., Zheng, J., Chen, Z., et al. (2019). Simultaneously dual modification of Ni-Rich layered oxide cathode for high-energy lithium-ion batteries. Adv. Funct. Mater. 29. https://doi.org/10.1002/adfm.201808825.

15. Cai, L., Liu, Z., An, K., and Liang, C. (2012). Probing Li-Ni Cation disorder in Li1−xNi1+x−yAlyO2Cathode materials by neutron diffraction. J. Electrochem. Soc. 159, A924–A928. https://doi.org/10.1149/2.005207jes.

16. Xiang, J., Chang, C., Yuan, L., and Sun, J. (2008). A simple and effective strategy to synthesize Al2O3-coated LiNi0.8Co0.2O2 cathode materials for lithium ion battery. Electrochem. Commun. 10, 1360–1363. https://doi.org/10.1016/j.elecom.2008.07.012.

17. Du, K., Xie, H., Hu, G., Peng, Z., Cao, Y., and Yu, F. (2016). Enhancing the thermal and upper voltage performance of Ni-Rich cathode material by a homogeneous and facile coating method: spray-drying coating with Nano-Al2O3. ACS Appl. Mater. Interfaces 8, 17713–17720. https://doi.org/10.1021/acsami.6b05629.

18. Park, M.H., Noh, M., Lee, S., Ko, M., Chae, S., Sim, S., Choi, S., Kim, H., Nam, H., Park, S., et al. (2014). Flexible high-energy Li-ion batteries with fast-charging capability. Nano Lett 14, 4083–4089. https://doi.org/10.1021/nl501597s.

19. Xiong, X., Wang, Z., Yan, G., Guo, H., and Li, X. (2014). Role of V2O5 coating on LiNiO2-based materials for lithium ion battery. J. Power Sources 245, 183–193. https://doi.org/10.1016/j.jpowsour.2013.06.133.

20. Schipper, F., Bouzaglo, H., Dixit, M., Erickson, E.M., Weigel, T., Talianker, M., Grinblat, J., Burstein, L., Schmidt, M., Lampert, J., et al. (2018). From surface ZrO2 coating to bulk Zr doping by high temperature annealing of nickel-rich lithiated oxides and their enhanced electrochemical performance in lithium ion batteries. Adv. Energy Mater. 8, 1701682. https://doi.org/10.1002/aenm.201701682.

21. Cho, J., Kim, T.-J., Kim, Y.J., and Park, B. (2001). High-performance ZrO2-coated LiNiO2 cathode material. Electrochem. Solid State Lett. 4, A159. https://doi.org/10.1149/1.1398556.

22. Hu, G.-R., Deng, X.-R., Peng, Z.-D., and Du, K. (2008). Comparison of AlPO4- and CO3(PO4)2-coated LiNi0.8Co0.2O2 cathode materials for Li-ion battery. Electrochim. Acta 53, 2567–2573. https://doi.org/10.1016/j.electacta.2007.10.040.

23. Min, K., Park, K., Park, S.Y., Seo, S.W., Choi, B., and Cho, E. (2017). Improved electrochemical properties of LiNi0.91Co0.06Mn0.03O2 cathode material via Li-reactive coating with metal phosphates. Sci. Rep. 7, 7151. https://doi.org/10.1038/s41598-017-07375-6.

24. Sun, Y.K., Myung, S.T., Shin, H.S., Bae, Y.C., and Yoon, C.S. (2006). Novel core− shell-structured Li [(Ni0. 8Co0. 2) 0.8 (Ni0. 5Mn0. 5) 0.2] O2 via coprecipitation as positive electrode material for lithium secondary batteries. J. Phys. Chem. B 110, 6810–6815.

25. Wu, F., Kim, G.T., Diemant, T., Kuenzel, M., Schür, A.R., Gao, X., Qin, B., Alwast, D., Jusys, Z., Behm, R.J., et al. (2020). Reducing capacity and voltage decay of Co-free Li 1.2 Ni 0.2 Mn 0.6 O 2 as positive electrode material for lithium batteries employing an ionic liquid-based electrolyte. Adv. Energy Mater. *10*, 2001830. https://doi.org/10.1002/aenm.202001830.

26. Montanino, M., Alessandrini, F., Passerini, S., and Appetecchi, G.B. (2013). Water-based synthesis of hydrophobic ionic liquids for high-energy electrochemical devices. Electrochim. Acta *96*, 124–133. https://doi.org/10.1016/j.electacta.2013.02.082.

27. Kühnel, R.-S., Lübke, M., Winter, M., Passerini, S., and Balducci, A. (2012). Suppression of aluminum current collector corrosion in ionic liquid containing electrolytes. J. Power Sources *214*, 178–184. https://doi.org/10.1016/j.jpowsour.2012.04.054.

28. Kim, U.-H., Kuo, L.-Y., Kaghazchi, P., Yoon, C.S., and Sun, Y.-K. (2019). Quaternary layered Ni-Rich NCMA cathode for lithium-ion batteries. ACS Energy Lett. *4*, 576–582. https://doi.org/10.1021/acsenergylett.8b02499.

29. Yoon, C.S., Park, K., Kim, U., Kang, K.H., Ryu, H., and Sun, Y. (2017). High-energy ni-rich Li [NixCoyMn1−x−y]O2 cathodes via compositional partitioning for next-generation electric vehicles. Chem. Mater. *29*, 10436–10445. https://doi.org/10.1021/acs.chemmater.7b04047.

30. Kim, J.-H., Kim, S.J., Yuk, T., Kim, J., Yoon, C.S., and Sun, Y.-K. (2018). Variation of electronic conductivity within secondary particles revealing a capacity-fading mechanism of layered Ni-Rich cathode. ACS Energy Lett. *3*, 3002–3007. https://doi.org/10.1021/acsenergylett.8b02043.

31. Li, J., Downie, L.E., Ma, L., Qiu, W., and Dahn, J.R. (2015). Study of the failure mechanisms of LiNi0.8Mn0.1Co0.1O2 cathode material for lithium ion batteries. J. Electrochem. Soc. *162*, A1401–A1408. https://doi.org/10.1149/2.1011507jes.

32. de Biasi, L., Schiele, A., Roca-Ayats, M., Garcia, G., Brezesinski, T., Hartmann, P., and Janek, J. (2019). Phase transformation behavior and stability of LiNiO2 cathode material for Li-ion batteries obtained from in situ gas analysis and operando X-ray diffraction. ChemSusChem *12*, 2240–2250. https://doi.org/10.1002/cssc.201900032.

33. Choi, J.U., Voronina, N., Sun, Y.K., and Myung, S.T. (2020). Recent progress and perspective of Advanced High-Energy Co-less Ni-Rich cathodes for Li-ion batteries: yesterday, today, and tomorrow. Adv. Energy Mater. *10*, 2002027. https://doi.org/10.1002/aenm.202002027.

34. Zhao, W., Zheng, J., Zou, L., Jia, H., Liu, B., Wang, H., Engelhard, M.H., Wang, C., Xu, W., Yang, Y., and Zhang, J.-G. (2018). High voltage operation of Ni-Rich NMC cathodes enabled by stable electrode/electrolyte interphases. Adv. Energy Mater. *8*, 1800297. https://doi.org/10.1002/aenm.201800297.

35. Alvarado, J., Schroeder, M.A., Pollard, T.P., Wang, X., Lee, J.Z., Zhang, M., Wynn, T., Ding, M., Borodin, O., Meng, Y.S., and Xu, K. (2019). Bisalt ether electrolytes: a pathway toward lithium metal batteries with Ni-rich cathodes. Energy Environ. Sci. *12*, 780–794. https://doi.org/10.1039/C8EE02601G.

36. Stich, M., Göttlinger, M., Kurniawan, M., Schmidt, U., and Bund, A. (2018). Hydrolysis of LiPF6 in carbonate-based electrolytes for lithium-ion batteries and in aqueous media. J. Phys. Chem. C *122*, 8836–8842. https://doi.org/10.1021/acs.jpcc.8b02080.

37. Solchenbach, S., Metzger, M., Egawa, M., Beyer, H., and Gasteiger, H.A. (2018). Quantification of PF5 and POF3 from side reactions of LiPF6 in Li-ion batteries. J. Electrochem. Soc. *165*, A3022–A3028. https://doi.org/10.1149/2.0481813jes.

38. Zheng, J., Liu, T., Hu, Z., Wei, Y., Song, X., Ren, Y., Wang, W., Rao, M., Lin, Y., Chen, Z., et al. (2016). Tuning of thermal stability in layered Li(NixMnyCoz)O2. J. Am. Chem. Soc. *138*, 13326–13334. https://doi.org/10.1021/jacs.6b07771.

39. Toby, B.H., and Von Dreele, R.B. (2013). GSAS-II: the genesis of a modern open-source all purpose crystallography software package. J. Appl. Crystallogr. *46*, 544–549. https://doi.org/10.1107/S0021889813003531.

40. Zheng, X., Li, X., Zhang, B., Wang, Z., Guo, H., Huang, Z., Yan, G., Wang, D., and Xu, Y. (2016). Enhanced electrochemical performance of LiNi0.8Co0.1Mn0.1O2 cathode materials obtained by atomization co-precipitation method. Ceramics International *42*, 644–649. https://doi.org/10.1016/j.ceramint.2015.08.159.